









Hole doping in a negative charge transfer insulator

Ranjan Kumar Patel ^{1,5}, Krishnendu Patra^{2,5}, Shashank Kumar Ojha ¹, Siddharth Kumar ¹, Sagar Sarkar ^{2,3}, Akash Saha¹, Nandana Bhattacharya¹, John W. Freeland ⁴, Jong-Woo Kim ⁴, Philip J. Ryan⁴, Priya Mahadevan ²✉ & Srimanta Middey ¹✉

$RENiO_3$ is a negative charge transfer energy system and exhibits a temperature-driven metal-insulator transition (MIT), which is also accompanied by a bond disproportionation (BD) transition. In order to explore how hole doping affects the BD transition, we have investigated the electronic structure of single-crystalline thin films of $Nd_{1-x}Ca_xNiO_3$ by synchrotron based experiments and ab-initio calculations. Here we show that for a small value of x , the doped holes are localized on one or more Ni sites around the dopant Ca^{2+} ions, while the BD state for the rest of the lattice remains intact. The effective charge transfer energy (Δ) increases with Ca concentration and the formation of BD phase is not favored above a critical x , suppressing the insulating phase. Our present study firmly demonstrates that the appearance of BD mode is essential for the MIT of the $RENiO_3$ series.

¹Department of Physics, Indian Institute of Science, Bengaluru 560012, India. ²S. N. Bose National Centre for Basic Sciences, Block-JD, Salt Lake, Kolkata 700106, India. ³Asia Pacific Center for Theoretical Physics, Pohang 37673, Korea. ⁴Advanced Photon Source, Argonne National Laboratory, Argonne, IL 60439, USA. ⁵These authors contributed equally: Ranjan Kumar Patel, Krishnendu Patra. ✉email: priya.mahadevan@gmail.com; smiddey@iisc.ac.in

The topic of metal-insulator transition (MIT) in transition metal (TM) compounds has remained at the forefront of condensed-matter physics research ever since its discovery as there are still some aspects that remain enigmatic¹. While one would have thought that by now, the issue of what drives the insulating state would have been settled, one still finds new regimes that bring up the question again, in addition to the fact that there is no single parameter that is the answer. Classifying the regimes in which one finds insulating states, the early TM oxides are driven insulating by strong electron-electron interactions (U) at the TM site, with the band gap scaling with the strength of U (ref. 2). This is not to say that electron correlation effects play no role among the late TM compounds. Their presence is necessary, though, here the charge transfer energy (Δ) between the ligand p and the TM d states is the scale that decides the magnitude of the band gap. This would suggest that a negative charge transfer energy where one has an overlap of the anion p and cation d bands would lead to a metallic state. While these ideas made up the Zaanen Sawatzky Allen phase diagram², a later extension that invoked the periodicity of the lattice found that even in this negative Δ regime, strong p - d hybridization between the anion p and TM d states can open up a band gap³. In spite of this regime being identified in the theoretical phase diagram, usually some other effects take over and very few systems so far have been identified as belonging to this covalent insulator regime^{4–6}.

In this work, we consider rare-earth nickelates $RENiO_3$ ($RE = Pr, Nd, Sm, \dots Lu, \text{etc.}$)^{7–11}, which are found to belong to this negative Δ regime^{4,12} and exhibit temperature driven simultaneous electronic and structural transitions. A magnetic transition also appears at the same temperature in $NdNiO_3$ and $PrNiO_3$. The insulating state is generally associated with the development of structural distortions, leading to the presence of two structurally inequivalent Ni atoms in the unit cell^{12–18}. The one with longer Ni–O bonds mimics the Ni^{2+} (d^8 ; $S = 1$) site, while the other with shorter Ni–O bonds mimics the Ni^{4+} ($d^8\bar{L}^2$; $S = 0$) site (\bar{L} represents a hole on oxygen). This is referred as a bond disproportionated (BD) phase, instead of a conventional charge disproportionated (CD) phase as there is no substantial charge difference between the two sites^{13–16}. It has been argued recently that the appearance of such BD phase in $RENiO_3$ is intimately connected with the negative Δ (ref. 19). On the other hand, one recent study claimed that the structure remains orthorhombic across the MIT²⁰.

Suppression/disentangling of the MIT has been examined recently in order to understand the origin of the simultaneous transitions of $RENiO_3$ ^{9,11,17,21–25}. Hole doping is another way to suppress the antiferromagnetic, insulating phase of $RENiO_3$ ^{26–28}. Surprisingly, very little is known about the nature of these doped holes and the underlying mechanism behind the absence of the MIT. The recent discovery of superconductivity in hole doped $NdNiO_2$ ²⁹, which lies at the boundary between the Mott-Hubbard and the charge transfer insulating regime^{30–33}, further demands the necessity of understanding the consequences of hole doping on the electronic structure in these complex materials. In contrast to conventional semiconductors³⁴, the insulating state among the transition metal oxides has been found to persist even up to 10–20% doping^{35–37}. Surprisingly, the nature of the insulating state in doped compositions is less characterized. In some cases, the doped holes are localized, leading to polaronic distortions or charge ordering. However, there is no single mechanism that can be ascribed to what preserves the insulating state. In this work, we consider the hole doped nickelates which have a BD state at the undoped limit to examine the consequences of hole doping. Addressing these issues will not only help us understand

the hole doping in negative charge transfer systems, but also can enable us to formulate guidelines for achieving unconventional superconductivity in the non-cuprate family.

We have grown a series of single crystalline $Nd_{1-x}Ca_xNiO_3$ thin films and investigated their structural and electronic behavior by transport measurements, synchrotron based X-ray diffraction (XRD), X-ray absorption spectroscopy (XAS), and resonant X-ray scattering (RXS). The appearance of a simultaneous BD transition with the MIT for the parent compound $NdNiO_3$ (NNO) has been confirmed by RXS experiments. The MIT temperature decreases with the Ca doping and vanishes around $x = 0.066$. Our density functional theory (DFT) based calculations carried out for small hole doping have found that instead of melting the bond ordered lattice, the doped holes are localized on one or more Ni^{2+} sites. This converts a Ni^{2+} site into a Ni^{3+} site, while the rest of the sites remain bond ordered. Our XAS measurements have revealed that the Ca doping leads to an increase in the value of Δ . However, the overall value of Δ still remains negative, which preserves the BD transition. A larger amount of Ca doping suppresses the BD transition as the energy cost associated with the localized holes (Ni^{3+} sites) also increases with x . The absence of BD transition has been confirmed by our RXS measurements on the entirely metallic film with $x = 0.1$ composition.

Results and discussion

Structural and electrical properties. 15 unit cell (u.c. in pseudo-cubic setting) $Nd_{1-x}Ca_xNiO_3$ epitaxial thin films with $x = 0, 0.02, 0.035, 0.05, 0.06, 0.066$ and 0.1 were grown on single crystalline $NdGaO_3$ ($1\ 1\ 0$)_{or} substrates [= ($0\ 0\ 1$)_{pc}, or and pc denote orthorhombic and pseudo-cubic setting, respectively] by a pulsed laser deposition (PLD) system. Fig. 1a shows a representative l scan along ($0\ 0\ 2$)_{pc} truncation rod using synchrotron X-ray diffraction for the $x = 0.1$ film (see Supplementary Note 2 for l scans of other samples). The diffraction patterns consist of a very sharp substrate peak, a broad film peak, and a set of thickness fringes, which arise due to the difference in the optical path of the X-ray in the film and the substrate. The out-of-plane lattice constant (c_{pc}) of these films decreases with the increase of Ca doping [inset of Fig. 1a] though the ionic radii of Ca^{2+} (1.12 Å) is slightly greater than that of Nd^{3+} (1.109 Å). This observation also strongly negates the presence of any oxygen vacancy, which would result in an increase in the lattice volume otherwise³⁸. This finding rather implies that the doped holes are located on Ni-sites^{39,40}.

Since the electronic behaviors of $RENiO_3$ are intimately connected with the underlying crystal symmetry, we have also investigated the structural symmetry of these films. The parent compound NNO is orthorhombic at room temperature. The observation of half order spots in reflection high energy electron diffraction (RHEED) images of all of these films (see Supplementary Note 1) suggest that these films have orthorhombic symmetry. The orthorhombic symmetry for the $x = 0.1$ film has been further confirmed by the presence [Fig. 1b] of ($0\ 1/2\ 2$)_{pc} diffraction peak (recorded using synchrotron X-ray), which arises due to the antiparallel displacement of A sites for orthorhombic ABO_3 perovskite^{17,41}. Moreover, the absence of ($1/2\ 0\ 2$)_{pc} peak for both film and substrate [Fig. 1b] ensures the film is structurally a single domain with the same in-plane doubling direction as the substrate, which is desired for X-ray scattering experiments - described in the latter part of this paper.

All bulk $RENiO_3$, having an orthorhombic phase in the metallic phase, undergo a temperature driven MIT. The resistivity of all $Nd_{1-x}Ca_xNiO_3$ films are very similar at room temperature

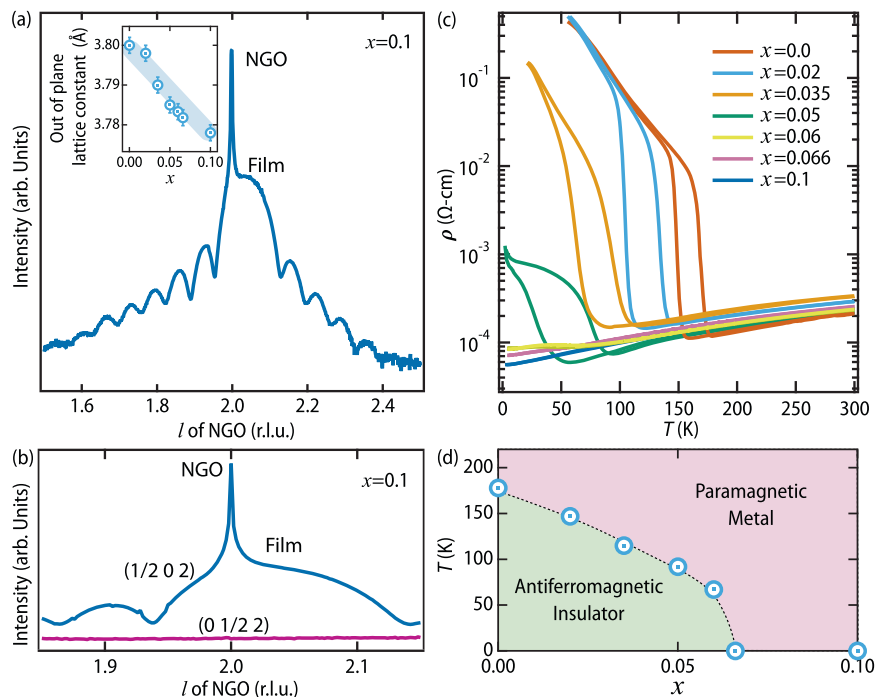


Fig. 1 Structural characterization and electronic properties. **a** l scan using X-ray diffraction of the $x = 0.1$ film through the $(0\ 0\ 2)_{pc}$ (pc denote pseudocubic setting) truncation rods. The change in the out-of-plane lattice constant with hole doping has been shown in the inset. The error bar is defined according to the step size of the l scan. The shaded region is a guide to the eye. **b** l scan of $x = 0.1$ sample around the $(0\ 1/2\ 2)_{pc}$ and $(1/2\ 0\ 2)_{pc}$ truncation rod at 300 K. **c** Temperature dependence of resistivity of Ca-doped NdNiO_3 films. The data for $x = 0$ film has been adapted from ref. 44. **d** Phase diagram of $\text{Nd}_{1-x}\text{Ca}_x\text{NiO}_3$ thin films. T_{MIT} (metal to insulator transition temperature) - T_N (paramagnetic to E' -AFM transition temperature) in heating run have been plotted as a function of x (hole doping). See Supplementary Note 3 for the details about the extraction of T_N from the transport data.

[Fig. 1c]. This further implies that the Ca doping does not incorporate oxygen vacancies in these films, which would lead to an increase of resistivity in the metallic phase³⁸. As reported earlier^{42–44}, NNO film on NGO undergoes a temperature driven first order MIT with a thermal hysteresis. The transition temperature in both heating (T_{MIT}^h) and cooling run (T_{MIT}^c) decreases monotonically with increasing Ca doping. However, the width of the hysteresis ($\delta T = T_{MIT}^h - T_{MIT}^c$), which represents the coexistence of metallic and insulating regions⁴⁵, increases with x . The insulating phase is completely absent in the $x = 0.066$ film. The paramagnetic to E' -AFM transition temperature (T_N) of RENiO_3 can be approximately found out by plotting $d(\ln\rho)/d(1/T)$ as a function of T (ref. 46). A similar analysis for these films with $x = 0, 0.02, 0.035, \text{ and } 0.05$ found $T_{MIT} \sim T_N$ (see Supplementary Note 3). The plot of T_{MIT}^h as a function of x [Fig. 1d] demonstrates the electronic phase diagram of Ca doped NNO films.

DFT calculations. To understand the evolution of the electronic structure with Ca doping, it is crucial to know the location of the doped hole. To examine this, we have performed ab-initio calculations considering E' -AFM state for the doping concentration of 0%, 3.125%, 6.25% and 9.375%. The system was found to be insulating for all cases. We do not attempt to find the point of the crossover between the insulating state to the metallic state in our calculations, as it is well known that the relative differences between different magnetic configurations are not correctly reproduced in DFT calculations at the undoped limit^{14,42,47,48}. The trends in the structural parameters, however, have been found to be well captured which has been the basis for examining the structural and electronic properties for the doped concentrations.

Considering the dopant concentration of 3.125%, we find that structural distortions about the different Ni atoms lead us to 3 inequivalent types of Ni atoms. These are differentiated by the bond lengths of the NiO_6 octahedra. The sites identified as Ni^{2+} have six long Ni–O bonds of length nearly 2.0 Å, while those identified as Ni^{4+} have six short Ni–O bonds of length nearly 1.9 Å. The Ni^{3+} sites are intermediate, with a combination of short and long bonds. Examining the Ni d projected density of states, we find that the Ni^{2+} sites have the states with t_{2g} symmetry filled up in the majority as well as the minority spin channel, while the states with e_g symmetry are filled in only the majority spin channel. This is shown in Fig. 2a–c with the unoccupied minority spin e_g states found in the energy window 3–4 eV above the Fermi level. The sites identified as Ni^{4+} however, have the t_{2g} states in both spin channels completely filled, while the states with e_g symmetry are completely unoccupied [Fig. 2b]. Most importantly, some of the Ni^{2+} sites around the Ca site are seen to convert to Ni^{3+} , with a splitting of the majority spin e_g states [Fig. 2c]. This is accompanied by a structural distortion [Fig. 2d], with four Ni–O bonds of the Ni^{3+} site becoming shorter, compared to what we had for the Ni^{2+} site. There are corresponding changes in the bond lengths of the neighboring Ni^{4+} sites as well to accommodate these changes. As a consequence of these distortions of the oxygens about the Ni^{3+} sites, the degenerate majority spin e_g orbitals split up, with the $d_{x^2-y^2}$ orbitals having higher energy than the $d_{3z^2-r^2}$. This is depicted schematically in Fig. 2e. Consequently, the doped hole is localized at the Ni^{3+} sites, with the system remaining insulating⁴⁹. The sites identified as Ni^{2+} , Ni^{3+} and Ni^{4+} have the same charge and can be differentiated with only their magnetic moments (the magnetic moments of Ni^{2+} , Ni^{3+} and Ni^{4+} are $1.5 \mu_B$, $0.98 \mu_B$ and $0 \mu_B$, respectively) as has been discussed earlier⁵⁰. The picture at the higher doping

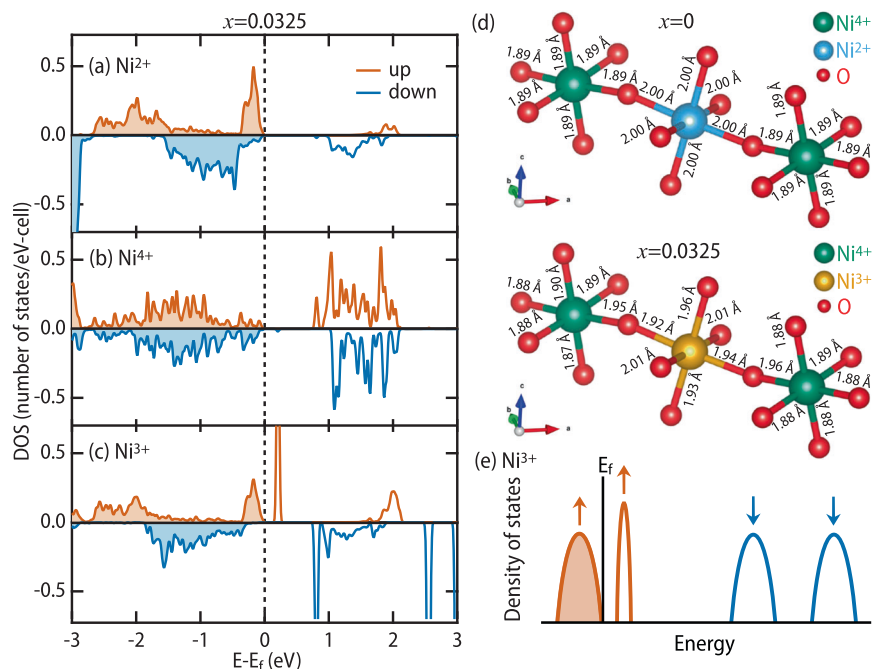


Fig. 2 **Ab initio** calculations. **a–c** Calculated spin resolved density of states of Ni²⁺, Ni⁴⁺, and Ni³⁺, respectively for $x = 0.0325$. **d** Ni–O bond lengths for $x = 0$ and $x = 0.0325$, respectively. The doped hole is going to one of the Ni²⁺ sites around the Ca dopant, converting it to Ni³⁺ (see Supplementary Note 4 for full relaxed structures). **e** Schematic of density of states of Ni³⁺ of $x = 0.0325$.

concentrations of 6.25% and 9.375% remains the same, with only more Ni²⁺ sites being converted to Ni³⁺, though the distortions of the Ni³⁺ sites may be different. We also note that such localized charge transfer has been also found in nickelate superlattice⁵¹.

The question that follows at this point is, why is the doped hole in Ca substituted NNO localized at a single Ni site, converting that to Ni³⁺, leaving the bond ordering of the rest of the lattice intact. This can be understood qualitatively by the following arguments. The hole doping is accompanied by a change in the electrostatic potential, which then goes on to modify the onsite energies, thereby changing Δ (ref. 1). When the hole is localized at the Ni³⁺ site, Δ is found to change by 0.29 eV from the value of Ni²⁺ site. A homogeneously distributed hole would lead to a change of 0.009 eV in the value of Δ , still keeping it in the negative Δ regime. This is the reason why the bond order is not destroyed upon hole doping and survives up to 9.375% doping as examined within our calculations. While our calculations examine an ordered distribution of the Ca dopant sites in the lattice, these may in reality be randomly distributed. This could lead to enhanced localization than what we find here. However, the gross features of the structural distortions and the electronic structure should follow through there. The aspects focusing on the randomness will be examined in future works.

Soft X-ray absorption spectroscopy. To investigate any change in Δ with Ca doping, we have measured XAS at the Ni $L_{3,2}$ -edges at 300 K (see Supplementary Note 5 for full spectra) using bulk-sensitive total fluorescence yield mode. The weak shoulder peak (around 853 eV) in the L_3 -edge of the parent compound becomes more prominent with the Ca doping [Fig. 3a]. Our analysis of the L_3 -edges⁵² has also found an increase in the peak separation energy with Ca incorporation [Fig. 3b]. While the XAS results for the insulating phase of RENiO₃ have been interpreted using double cluster calculations in recent times¹⁸, single-site cluster calculations can still be used to understand the change in XAS in the metallic phase where all Ni sites are equivalent. According to

the results of single-site cluster calculations^{52–54}, the increase in the peak separation of L_3 edge by 0.09 eV from $x = 0$ to $x = 0.1$ sample would correspond to ~ 0.3 eV increase of Δ . This change in Δ would decrease the covalency between Ni d and O p states. This is further corroborated by the measurement of O K -edge XAS (see Supplementary Note 5 for full spectra), where a pre-peak arises around 528.5 eV [Fig. 3c] due to the $d^8\bar{L} \rightarrow cd^8$ transition (\bar{L} denotes a core hole in O 1s core level). The intensity of the pre-peak, which is a measure of the contribution of the $d^8\bar{L}$ configuration, decreases with Ca doping in NNO [Fig. 3d]. We believe that the increase of Δ with Ca doping is related to the increase of (Nd, Ca)-O covalency⁵⁵.

Resonant hard X-ray scattering. Based on these experimental and theoretical results, we propose the following situations. For a small amount of Ca doping, the effective Δ is still negative, and the system undergoes a BD insulating phase with the lowering of temperature¹⁹. With the increase of x , Δ increases and the appearance of BD phase is prohibited above a critical value. Consequently, the sample remains metallic down to low temperature. In order to confirm this, we have performed temperature dependent RXS experiments on the $x = 0$ and 0.1 films. Such RXS experiments around the $(0\ k\ l)_{\text{or}}$ and $(h\ 0\ l)_{\text{or}}$ reflections (h, k, l : odd integers) with the energy tuned to Ni K -edge ($1s \rightarrow 4p$ transition) were employed earlier to detect CD/BD transition of several RENiO₃ thin films and heterostructures^{17,46,56–61}. The intensity of the $(0\ 1\ 1)_{\text{or}} \equiv (-1/2\ 1/2\ 1/2)_{\text{pc}}$ reflection for Nd_{1-x}Ca_xNiO₃ films is given by $I_{011}(\mathbf{Q}, E) \propto A_{\text{O,Nd/Ca}}^2(\mathbf{Q}) + 2A_{\text{O,Nd/Ca}}(\mathbf{Q}) \cdot 2(\Delta f_{\text{Ni}}^0(\mathbf{Q}) + \Delta f'_{\text{Ni}}(E) + \Delta f''_{\text{Ni}}(E)) + 4(\Delta f_{\text{Ni}}^0(\mathbf{Q}) + \Delta f'_{\text{Ni}}(E) + \Delta f''_{\text{Ni}}(E))^2$ ^{17,46}, where $\Delta f_{\text{Ni}}^0(\mathbf{Q}) = [f_{\text{Ni1}}^0(\mathbf{Q}) - f_{\text{Ni2}}^0(\mathbf{Q})]$, $\Delta f'_{\text{Ni}}(E) = [f'_{\text{Ni1}}(E) - f'_{\text{Ni2}}(E)]$ and $\Delta f''_{\text{Ni}}(E) = [f''_{\text{Ni1}}(E) - f''_{\text{Ni2}}(E)]$. Energy-independent Thompson scattering (TS) terms are represented by the term $A_{\text{O,Nd/Ca}}(\mathbf{Q})[f_{\text{Ni}}^0(\mathbf{Q})]$ for Nd/Ca and O [Ni] sites. As the energy-dispersive correction factors for the Ni sites: $f'_{\text{Ni}}(E)$ (real part) and $f''_{\text{Ni}}(E)$ (imaginary part) are vanishingly small for an

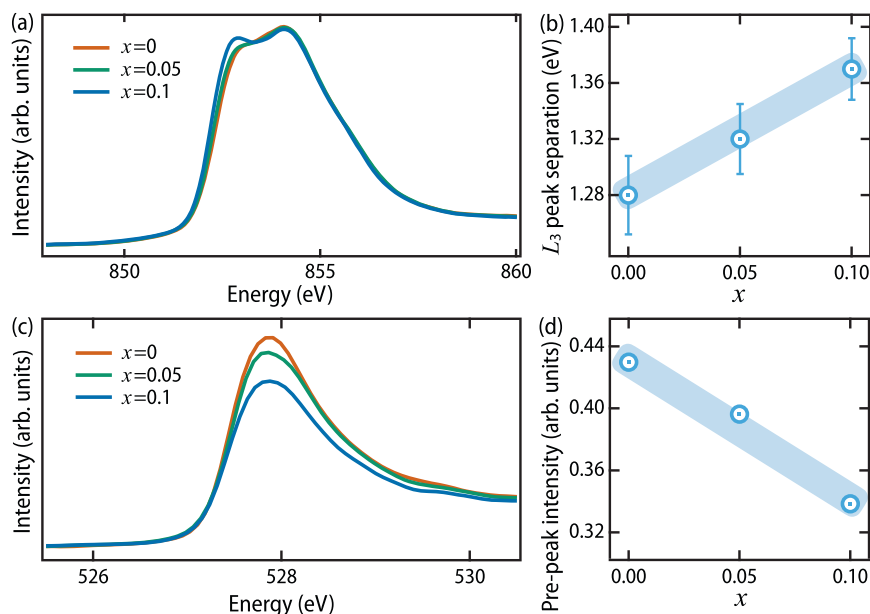


Fig. 3 X-ray absorption spectroscopy. **a** Normalized X-ray absorption spectra at Ni L_3 -edge. **b** The energy separation between the two peaks of the L_3 -edge for $x = 0, 0.05,$ and 0.1 thin films. The error bar is defined from the errors in the peak position while fitting the two peaks of the Ni L_3 -edge. **c** K -edge XAS pre-peak and **d** the pre-peak intensity as a function of Ca doping. The shaded regions in **b** and **d** are guide to the eye.

energy few eV away from the resonance edge, recording of $(-1/2 \ 1/2 \ 1/2)_{pc}$ reflection using X-ray with off-resonant energy can also probe BD, which is a pure structural effect⁶¹. While the $(-1/2 \ 1/2 \ 1/2)_{pc}$ reflection is forbidden in the orthorhombic phase of $RENiO_3$, we observed a small intensity for this reflection at 300 K for the NNO film [Fig. 4a]. This arises due to the contribution of the off-diagonal elements of the energy-dispersive scattering factors⁵⁹. The reflection is much stronger at 4 K, as expected for the presence of BD in the insulating phase. The intensity of this reflection does not change with lowering T for the film with $x = 0.1$ [Fig. 4b], signifying the entire suppression of the periodic BD ordering by 10% Ca doping.

The above conclusions have been further validated by energy scans across the Ni K -edge for the $(-1/2 \ 1/2 \ 1/2)_{pc}$ reflection. In the metallic phase of the NNO film, we observe some energy dependence [Fig. 4c] due to the octahedral tilt, akin to the recent reports on NNO film⁵⁹ and $1EuNiO_3/1LaNiO_3$ superlattice¹⁷. The increase in the off-resonant intensity [Fig. 4c, d] across the MIT testifies a simultaneous BD transition. Unlike the earlier reports of charge ordering in thick NNO film⁵⁶ and $1EuNiO_3/1LaNiO_3$ superlattice¹⁷, our 6 nm thin NNO film does not exhibit a large increase in the intensity at the resonant energy in its insulating phase [Fig. 4c]. We further emphasize that the BD, which involves electronic rearrangement within the oxygen sublattice, can also drive a small electron disproportionation within the Ni sublattice^{18,46,61}. The small increase of the intensity at the resonance energy in the insulating phase [Fig. 4c, d] supports such a scenario. In the case of $x = 0.1$ film, the small resonance profile does not change across the temperature of our measurements, confirming the absence of any BD ordering [Fig. 4e]. These experimental results demonstrate that the p - p gap of a covalent insulator^{3,4} vanishes when the BD is absent and hence, the system becomes metallic. This settles a long standing issue regarding the coupling among structural effects and MIT of $RENiO_3$ and further implies that the electronic and structural order parameter should be considered together to describe the simultaneous transitions of the rare-earth nickelate series^{17,25,62–65}.

Conclusions

To summarize, we have investigated the electronic and structural behavior of a series of $Nd_{1-x}Ca_xNiO_3$ thin films using advanced synchrotron measurements and DFT calculations. We have observed that the partial replacement of Nd by Ca not only dopes holes in the system but also increases Δ gradually. As the BD emerges for negative Δ , an increase in Δ is expected to push the system away from the BD state even at small Ca doping. We find from DFT that the changes in Δ with respect to the undoped limit is not the same for each Ni site. Rather than disrupting the BD state even for small x , we find that one or more Ni^{2+} sites become Ni^{3+} . This could emerge from the large structural energy cost involved in losing the BD state, in addition to the large exchange splitting that exists for the Ni^{2+} sites. However, the energy cost associated with the polaronic distortion also enhances with x and eventually favors delocalized doped holes above a critical Ca doping concentration.

Finally, we would like to emphasize that the nature of hole doping in perovskite nickelate is very different compared to that in superconducting infinite-layer nickelates. While the hole doping results in an increase of $d^9\bar{L}$ state in hole doped $NdNiO_2$ (ref. 31), we have found a suppression of $d^8\bar{L}$ configuration in $NdNiO_3$, which might be responsible for the absence of the superconducting phase in the hole doped perovskite nickelates.

Methods

Sample preparation and measurements. All the polycrystalline targets were prepared by the liquid-mix technique⁴⁴. Stoichiometric amounts of $Ni(NO_3)_2 \cdot 6H_2O$ and citric acid (1:2 molar ratio) were added to deionized water and stirred at 70 °C for 30 min. Then, calculated amounts of analytical grade $Ca(NO_3)_2 \cdot 4H_2O$ and Nd_2O_3 were added to the solution. All the chemicals were obtained from Sigma Aldrich. The solution was stirred for another 30 min and the temperature was raised to 90 °C. The solution was kept at 90 °C and stirred until a gel was formed. After forming the gel, it was dried and calcinated in a furnace at 300 °C. The powders that formed after calcination was grounded and heated at 700 °C several times for better homogeneity under the flow of high pure oxygen. Finally, pellets were made from the powders and were annealed at 700 °C for 24 h. The films were grown on $NdGaO_3$ substrates by a Neocera pulsed laser deposition system (PLD), connected with an in-situ RHEED (Staib Instruments, Germany). A KrF excimer laser was used for the depositions operating with 2 Hz. The laser fluence was 1.5 J cm^{-2} and the depositions were done at a temperature of 735 °C under a dynamic

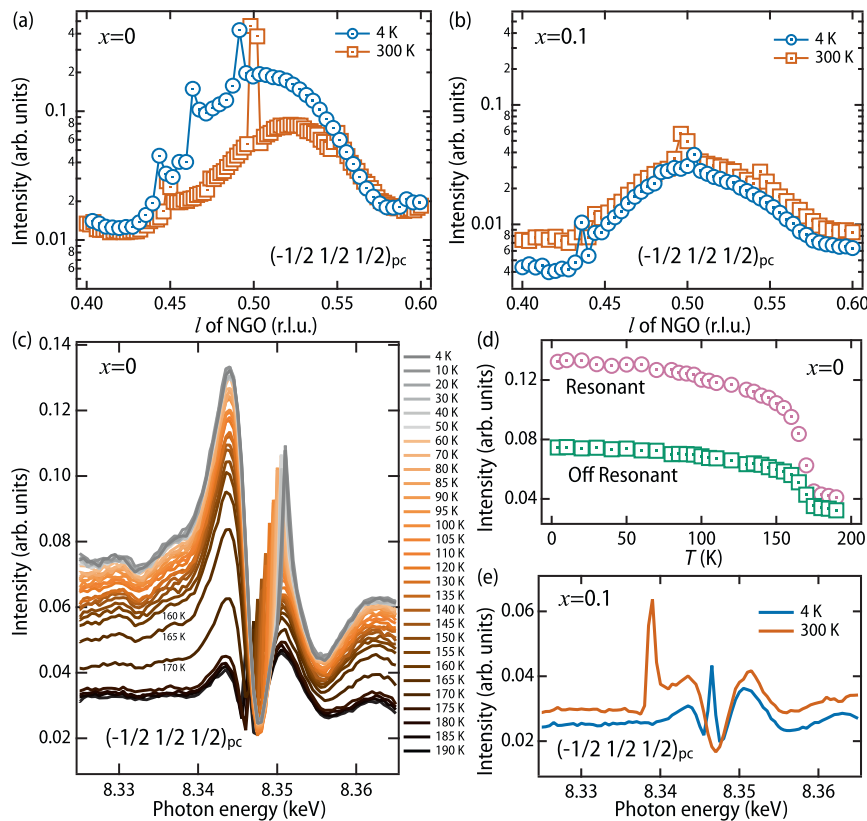


Fig. 4 Temperature dependent resonant X-ray scattering. l -scan through the $(-1/2\ 1/2\ 1/2)_{pc}$ [$(0\ 11)_{orr}$, or pc denote orthorhombic and pseudo-cubic setting, respectively] reflection for (a) $x=0$ and (b) $x=0.1$ thin films at 4 K and 300 K, recorded with photon energy 8.33 eV. The variation of the $(-1/2\ 1/2\ 1/2)_{pc}$ reflection of the $x=0$ thin film around Ni K-edge at various temperatures for (c) $x=0$ and (e) $x=0.1$ thin films. Temperature dependent resonant and off-resonant intensities (I_{res} and I_{offres}) of the corresponding scan of $x=0$ film are plotted in d. The spikes in a, b, c, and e arise due to multiple waves diffraction.

oxygen pressure of 150 mTorr. After finishing the deposition, all samples were post annealed at the growth temperature in an oxygen atmosphere of 500 torr for 30 min and cooled down to room temperature at a rate of $15^\circ\text{C}\ \text{min}^{-1}$.

Laboratory-based X-ray diffraction patterns were recorded using a laboratory-based Rigaku Smartlab diffractometer and the synchrotron XRD measurements were carried out at the Indian Beamline, Photon Factory, KEK, Japan. The electrical transport properties of these samples were measured in four probe Van der Pauw geometry in an Oxford Integra LLD system and all the contacts were made by using silver paint. XAS and RXS measurements were carried out at 4-ID-C and 6-ID-B beam-line, respectively in Advanced Photon Source (APS), Argonne National Laboratory, USA.

DFT calculations. The DFT calculations have been carried out by imposing the non collinear E' -type antiferromagnetic (E' -AFM) structure on the Ni sites in NdNiO_3 (ref. 66). Nd atoms have then been replaced by Ca atoms in an 160 atom supercell ($2\sqrt{2} \times 2\sqrt{2} \times 2$) corresponding to the doping concentrations of 3.125%, 6.25%, and 9.375%. The electronic structure was then calculated within a projected augmented wave⁶⁷ implementation of density functional theory within the Vienna ab-initio simulation package (VASP) code^{68–70}. We have used the generalized gradient approximation (GGA) for the exchange correlation functional⁷¹. Electron-electron interaction effects were included on the d orbitals at the Ni site, considering a value of U of 4 eV within the Dudarev implementation of $\text{GGA} + U$ ⁷². The lattice parameters were fixed at the experimental values^{73,74}, the internal positions were optimized till the forces were $<10^{-3}\ \text{eV}/\text{\AA}$. We used Monkhorst-Pack⁷⁵ k -points grid of $2 \times 2 \times 1$ for the calculations. A cutoff energy of 400 eV was used for the plane wave basis states included in the calculations. The density of states and magnetic moments were calculated by considering spheres of radii 1 Å around each atom, a distance which represents almost half the Ni–O bond length. The changes in Δ on doping are quantified by changes in the electrostatic potential at the Ni and O sites.

Data availability

The data of the results presented in this paper, including those in the Supplementary Information, are available from the corresponding authors upon reasonable request.

Received: 16 February 2022; Accepted: 8 August 2022;

Published online: 27 August 2022

References

- Imada, M., Fujimori, A. & Tokura, Y. Metal-insulator transitions. *Rev. Mod. Phys.* **70**, 1039–1263 (1998).
- Zaanen, J., Sawatzky, G. A. & Allen, J. W. Band gaps and electronic structure of transition-metal compounds. *Phys. Rev. Lett.* **55**, 418–421 (1985).
- Nimkar, S., Sarma, D. D., Krishnamurthy, H. R. & Ramasesha, S. Mean-field results of the multiple-band extended Hubbard model for the square-planar CuO_2 lattice. *Phys. Rev. B* **48**, 7355–7363 (1993).
- Barman, S. R., Chainani, A. & Sarma, D. D. Covalency-driven unusual metal-insulator transition in nickelates. *Phys. Rev. B* **49**, 8475–8478 (1994).
- Maiti, K., Sarma, D. D., Mizokawa, T. & Fujimori, A. Electronic structure of one-dimensional cuprates. *Phys. Rev. B* **57**, 1572–1578 (1998).
- Matsumo, J. et al. Different routes to charge disproportionation in perovskite-type Fe oxides. *Phys. Rev. B* **66**, 193103 (2002).
- Medarde, M. L. Structural, magnetic and electronic properties of RNiO_3 perovskites (R = rare earth). *J. Phys.: Condens. Matter* **9**, 1679 (1997).
- Catalan, G. Progress in perovskite nickelate research. *Phase Transit.* **81**, 729–749 (2008).
- Middey, S. et al. Physics of ultrathin films and heterostructures of rare-earth nickelates. *Annu. Rev. Mater. Res.* **46**, 305–334 (2016).
- Catalano, S. et al. Rare-earth nickelates RNiO_3 : thin films and heterostructures. *Rep. Prog. Phys.* **81**, 046501 (2018).
- Chakhalian, J. & Middey, S. Perspective—emergent phases in rare earth nickelate heterostructure. *ECS J. Solid State Sci. Technol.* **11**, 053004 (2022).
- Bisogni, V. et al. Ground-state oxygen holes and the metal–insulator transition in the negative charge-transfer rare-earth nickelates. *Nat. Commun.* **7**, 13017 (2016).
- Mizokawa, T., Khomskii, D. I. & Sawatzky, G. A. Spin and charge ordering in self-doped mott insulators. *Phys. Rev. B* **61**, 11263–11266 (2000).
- Park, H., Millis, A. J. & Marianetti, C. A. Site-selective mott transition in rare-earth-element nickelates. *Phys. Rev. Lett.* **109**, 156402 (2012).

15. Johnston, S., Mukherjee, A., Elfmov, I., Berciu, M. & Sawatzky, G. A. Charge disproportionation without charge transfer in the rare-earth-element nickelates as a possible mechanism for the metal-insulator transition. *Phys. Rev. Lett.* **112**, 106404 (2014).
16. Haule, K. & Pascut, G. L. Mott transition and magnetism in rare earth nickelates and its fingerprint on the x-ray scattering. *Sci. Rep.* **7**, 2045–2322 (2017).
17. Middey, S. et al. Disentangled cooperative orderings in artificial rare-earth nickelates. *Phys. Rev. Lett.* **120**, 156801 (2018).
18. Green, R. J., Haverkort, M. W. & Sawatzky, G. A. Bond disproportionation and dynamical charge fluctuations in the perovskite rare-earth nickelates. *Phys. Rev. B* **94**, 195127 (2016).
19. Mandal, B. et al. The driving force for charge ordering in rare earth nickelates. *arXiv* <https://doi.org/10.48550/arXiv.1701.06819> (2017).
20. Serrano-Sánchez, F., Martínez, J. L., Fauth, F. & Alonso, J. A. On the lack of monoclinic distortion in the insulating regime of EuNiO_3 and GdNiO_3 perovskites by high-angular resolution synchrotron x-ray diffraction: a comparison with YNiO_3 . *Dalton Trans.* **50**, 7085–7093 (2021).
21. Hepting, M. et al. Tunable charge and spin order in PrNiO_3 thin films and superlattices. *Phys. Rev. Lett.* **113**, 227206 (2014).
22. Stewart, M. K., Liu, J., Kareev, M., Chakhalian, J. & Basov, D. N. Mott physics near the insulator-to-metal transition in NdNiO_3 . *Phys. Rev. Lett.* **107**, 176401 (2011).
23. Ojha, S. K. et al. Anomalous electron transport in epitaxial NdNiO_3 films. *Phys. Rev. B* **99**, 235153 (2019).
24. Stoica, V. et al. Disentangling electronic and magnetic order in NdNiO_3 at ultrafast timescales. *arXiv* <https://doi.org/10.48550/arXiv.2004.03694> (2020).
25. Georgescu, A. B., Peil, O. E., Disa, A. S., Georges, A. & Millis, A. J. Disentangling lattice and electronic contributions to the metal-insulator transition from bulk vs. layer confined RNiO_3 . *Proc. Natl Acad. Sci. USA* **116**, 14434–14439 (2019).
26. Cheong, S.-W., Hwang, H., Batlogg, B., Cooper, A. & Canfield, P. Electron-hole doping of the metal-insulator transition compound RENiO_3 . *Phys. B: Condens. Matter* **194**, 1087–1088 (1994).
27. García-Muñoz, J., Suaaidi, M., Martínez-Lope, M. & Alonso, J. Influence of carrier injection on the metal-insulator transition in electron- and hole-doped $\text{R}_{1-x}\text{A}_x\text{NiO}_3$ perovskites. *Phys. Rev. B* **52**, 13563 (1995).
28. Xiang, P.-H. et al. Room temperature mott metal-insulator transition and its systematic control in $\text{Sm}_{1-x}\text{Ca}_x\text{NiO}_3$ thin films. *Appl. Phys. Lett.* **97**, 032114 (2010).
29. Li, D. et al. Superconductivity in an infinite-layer nickelate. *Nature* **572**, 624–627 (2019).
30. Jiang, M., Berciu, M. & Sawatzky, G. A. Critical nature of the Ni spin state in doped NdNiO_2 . *Phys. Rev. Lett.* **124**, 207004 (2020).
31. Goode, B. H. et al. Doping evolution of the mott-hubbard landscape in infinite-layer nickelates. *Proc. Natl Acad. Sci. USA* **118**, e2007683118 (2021).
32. Hepting, M. et al. Electronic structure of the parent compound of superconducting infinite-layer nickelates. *Nat. Mater.* **19**, 381–385 (2020).
33. Rossi, M. et al. Orbital and spin character of doped carriers in infinite-layer nickelates. *Phys. Rev. B* **104**, L220505 (2021).
34. Yamanouchi, C., Mizuguchi, K. & Sasaki, W. Electric conduction in phosphorus doped silicon at low temperatures. *J. Phys. Soc. Jpn.* **22**, 859–864 (1967).
35. Chainani, A., Mathew, M. & Sarma, D. D. Electron-spectroscopy study of the semiconductor-metal transition in $\text{La}_{1-x}\text{Sr}_x\text{CoO}_3$. *Phys. Rev. B* **46**, 9976–9983 (1992).
36. Chainani, A., Mathew, M. & Sarma, D. D. Electron spectroscopic investigation of the semiconductor-metal transition in $\text{La}_{1-x}\text{Sr}_x\text{MnO}_3$. *Phys. Rev. B* **47**, 15397–15403 (1993).
37. Katsufuji, T., Taguchi, Y. & Tokura, Y. Transport and magnetic properties of a mott-hubbard system whose bandwidth and band filling are both controllable: $\text{R}_{1-x}\text{Ca}_x\text{TiO}_{3+y/2}$. *Phys. Rev. B* **56**, 10145–10153 (1997).
38. Nikulin, I., Novojilov, M., Kaul, A., Mudretsova, S. & Kondrashov, S. Oxygen nonstoichiometry of $\text{NdNiO}_{3-\delta}$ and $\text{SmNiO}_{3-\delta}$. *Mater. Res. Bull.* **39**, 775–791 (2004).
39. Liu, J. et al. Tuning the electronic structure of LaNiO_3 through alloying with strontium to enhance oxygen evolution activity. *Adv. Sci.* **6**, 1901073 (2019).
40. Tan, Z., Heald, S. M., Cheong, S.-W., Cooper, A. S. & Moodenbaugh, A. R. Nature of hole doping in Nd_2NiO_4 and La_2NiO_4 : comparison with La_2CuO_4 . *Phys. Rev. B* **47**, 12365–12368 (1993).
41. Middey, S. et al. Phase engineering of rare earth nickelates by digital synthesis. *Appl. Phys. Lett.* **113**, 081602 (2018).
42. Liu, J. et al. Heterointerface engineered electronic and magnetic phases of NdNiO_3 thin films. *Nat. Commun.* **4**, 2714 (2013).
43. Mikheev, E. et al. Tuning bad metal and non-fermi liquid behavior in a mott material: rare-earth nickelate thin films. *Sci. Adv.* **1**, e1500797 (2015).
44. Patel, R. K. et al. Epitaxial stabilization of ultra thin films of high entropy perovskite. *Appl. Phys. Lett.* **116**, 071601 (2020).
45. Alsaqqa, A. M. et al. Phase coexistence and dynamical behavior in NdNiO_3 ultrathin films. *Phys. Rev. B* **95**, 125132 (2017).
46. Patel, R. K. et al. Emergent behavior of LaNiO_3 in short-periodic nickelate superlattices. *APL Mater.* **8**, 041113 (2020).
47. Gou, G., Grinberg, I., Rappe, A. M. & Rondinelli, J. M. Lattice normal modes and electronic properties of the correlated metal LaNiO_3 . *Phys. Rev. B* **84**, 144101 (2011).
48. Hampel, A. & Ederer, C. Interplay between breathing mode distortion and magnetic order in rare-earth nickelates RNiO_3 within DFT + U. *Phys. Rev. B* **96**, 165130 (2017).
49. Iglesias, L., Bibes, M. & Varignon, J. First-principles study of electron and hole doping effects in perovskite nickelates. *Phys. Rev. B* **104**, 035123 (2021).
50. Mahadevan, P., Terakura, K. & Sarma, D. D. Spin, charge, and orbital ordering in $\text{La}_{0.5}\text{Sr}_{1.5}\text{MnO}_4$. *Phys. Rev. Lett.* **87**, 066404 (2001).
51. Wang, L. et al. Hole-trapping-induced stabilization of Ni 4+ in $\text{SrNiO}_3/\text{LaFeO}_3$ superlattices. *Adv. Mater.* **32**, 2005003 (2020).
52. Liu, J. et al. Quantum confinement of mott electrons in ultrathin $\text{LaNiO}_3/\text{LaAlO}_3$ superlattices. *Phys. Rev. B* **83**, 161102 (2011).
53. Freeland, J. W., van Veenendaal, M. & Chakhalian, J. Evolution of electronic structure across the rare-earth RNiO_3 series. *J. Electron Spectrosc. Relat. Phenom.* **208**, 56–62 (2016).
54. Meyers, D. et al. Strain-modulated mott transition in EuNiO_3 ultrathin films. *Phys. Rev. B* **88**, 075116 (2013).
55. Singh, R. S. & Maiti, K. Manifestation of screening effects and A–O covalency in the core level spectra of a site elements in the ABO_3 structure of $\text{Ca}_{1-x}\text{Sr}_x\text{RuO}_3$. *Phys. Rev. B* **76**, 085102 (2007).
56. Staub, U. et al. Direct observation of charge order in an epitaxial NdNiO_3 film. *Phys. Rev. Lett.* **88**, 126402 (2002).
57. Lorenzo, J. E. et al. Resonant x-ray scattering experiments on electronic orderings in NdNiO_3 single crystals. *Phys. Rev. B* **71**, 045128 (2005).
58. Scagnoli, V. et al. Charge disproportionation and search for orbital ordering in NdNiO_3 by use of resonant x-ray diffraction. *Phys. Rev. B* **72**, 155111 (2005).
59. Lu, Y. et al. Quantitative determination of bond order and lattice distortions in nickel oxide heterostructures by resonant x-ray scattering. *Phys. Rev. B* **93**, 165121 (2016).
60. Meyers, D. et al. Charge order and antiferromagnetism in epitaxial ultrathin films of EuNiO_3 . *Phys. Rev. B* **92**, 235126 (2015).
61. Kim, J.-W. et al. Direct evidence of the competing nature between electronic and lattice breathing order in rare-earth nickelates. *Phys. Rev. Lett.* **124**, 127601 (2020).
62. Mercy, A., Bieder, J., Íñiguez, J. & Ghosez, P. Structurally triggered metal-insulator transition in rare-earth nickelates. *Nat. Commun.* **8**, 1677 (2017).
63. Hampel, A., Liu, P., Franchini, C. & Ederer, C. Energetics of the coupled electronic-structural transition in the rare-earth nickelates. *npj Quantum Mater.* **4**, 5 (2019).
64. Peil, O. E., Hampel, A., Ederer, C. & Georges, A. Mechanism and control parameters of the coupled structural and metal-insulator transition in nickelates. *Phys. Rev. B* **99**, 245127 (2019).
65. Georgescu, A. B. & Millis, A. J. Quantifying the role of the lattice in metal-insulator phase transitions. *Commun. Phys.* **5**, 135 (2022).
66. Scagnoli, V. et al. Role of magnetic and orbital ordering at the metal-insulator transition in NdNiO_3 . *Phys. Rev. B* **73**, 100409 (2006).
67. Blöchl, P. E. Projector augmented-wave method. *Phys. Rev. B* **50**, 17953–17979 (1994).
68. Kresse, G. & Hafner, J. Ab initio molecular dynamics for liquid metals. *Phys. Rev. B* **47**, 558–561 (1993).
69. Kresse, G. & Hafner, J. Ab initio molecular-dynamics simulation of the liquid-metal-amorphous-semiconductor transition in germanium. *Phys. Rev. B* **49**, 14251–14269 (1994).
70. Kresse, G. & Furthmüller, J. Efficient iterative schemes for ab initio total-energy calculations using a plane-wave basis set. *Phys. Rev. B* **54**, 11169–11186 (1996).
71. Perdew, J. P., Burke, K. & Ernzerhof, M. Generalized gradient approximation made simple. *Phys. Rev. Lett.* **77**, 3865–3868 (1996).
72. Dudarev, S. L., Botton, G. A., Savrasov, S. Y., Humphreys, C. J. & Sutton, A. P. Electron-energy-loss spectra and the structural stability of nickel oxide: An LSDA+U study. *Phys. Rev. B* **57**, 1505–1509 (1998).
73. García-Muñoz, J. L., Aranda, M. A. G., Alonso, J. A. & Martínez-Lope, M. J. Structure and charge order in the antiferromagnetic band-insulating phase of NdNiO_3 . *Phys. Rev. B* **79**, 134432 (2009).
74. García-Muñoz, J. L., Suaaidi, M., Martínez-Lope, M. J. & Alonso, J. A. Influence of carrier injection on the metal-insulator transition in electron- and hole-doped $\text{R}_{1-x}\text{A}_x\text{NiO}_3$ perovskites. *Phys. Rev. B* **52**, 13563–13569 (1995).
75. Monkhorst, H. J. & Pack, J. D. Special points for brillouin-zone integrations. *Phys. Rev. B* **13**, 5188–5192 (1976).

Acknowledgements

R.K.P. acknowledges XRD facility at the Department of Physics, IISc Bangalore. S.M. acknowledges a SERB Early Career Research Award (ECR/2018/001512) and a DST

Nanomission grant (Grant No. DST/NM/NS/2018/246) for funding. P.M. acknowledges SERB for funding through SPF/2021/000066. S.M., J.W.F., and P.M. are supported by Indo-US Joint Centre for Rational Engineering of Quantum Materials under Indo-U.S. Science and Technology Forum. This research used resources of the Advanced Photon Source, a U.S. Department of Energy Office of Science User Facility operated by Argonne National Laboratory under Contract No. DE-AC02-06CH11357.

Author contributions

S.M. conceived and designed the experiments. R.K.P. grew the Ca doped NNO samples with assistance from S.K.O., and S.M. XRD were done by S.K., and R.K.P. Temperature dependent resistivity measurements were done by R.K.P. A.S. and N.B. contributed in the synthesis of 6% and 6.6% Ca doped NdNiO₃ during the review of this paper. XAS measurements were carried out by R.K.P., and J.W.F. J.W.K. and P.J.R. did the X-ray scattering experiments. Analysis of all experimental data were done by R.K.P. under the supervision of S.M. The density functional theory calculations and theoretical guidance were provided by K.P., S.S., and P.M. All authors contributed in data interpretation. R.K.P., S.M., and P.M. wrote the paper with inputs from all authors.

Competing interests

The authors declare no competing interests.

Additional information

Supplementary information The online version contains supplementary material available at <https://doi.org/10.1038/s42005-022-00993-1>.

Correspondence and requests for materials should be addressed to Priya Mahadevan or Srimanta Middey.

Peer review information *Communications Physics* thanks the anonymous reviewers for their contribution to the peer review of this work.

Reprints and permission information is available at <http://www.nature.com/reprints>

Publisher's note Springer Nature remains neutral with regard to jurisdictional claims in published maps and institutional affiliations.



Open Access This article is licensed under a Creative Commons Attribution 4.0 International License, which permits use, sharing, adaptation, distribution and reproduction in any medium or format, as long as you give appropriate credit to the original author(s) and the source, provide a link to the Creative Commons license, and indicate if changes were made. The images or other third party material in this article are included in the article's Creative Commons license, unless indicated otherwise in a credit line to the material. If material is not included in the article's Creative Commons license and your intended use is not permitted by statutory regulation or exceeds the permitted use, you will need to obtain permission directly from the copyright holder. To view a copy of this license, visit <http://creativecommons.org/licenses/by/4.0/>.

© The Author(s) 2022